

NEURAL SOLVER FOR WASSERSTEIN GEODESICS AND OPTIMAL TRANSPORT DYNAMICS

YAN-HAN CHEN AND HAILIANG LIU

ABSTRACT. In recent years, the machine learning community has increasingly embraced the optimal transport (OT) framework for modeling distributional relationships. In this work, we introduce a sample-based neural solver for computing the Wasserstein geodesic between a source and target distribution, along with the associated velocity field. Building on the dynamical formulation of the optimal transport (OT) problem, we recast the constrained optimization as a minimax problem, using deep neural networks to approximate the relevant functions. This approach not only provides the Wasserstein geodesic but also recovers the OT map, enabling direct sampling from the target distribution. By estimating the OT map, we obtain velocity estimates along particle trajectories, which in turn allow us to learn the full velocity field. The framework is flexible and readily extends to general cost functions, including the commonly used quadratic cost. We demonstrate the effectiveness of our method through experiments on both synthetic and real datasets.

1. INTRODUCTION

In recent years, the machine learning community has shown growing interest in the optimal transport (OT) framework [54], which seeks to determine the most cost-effective transformation between probability distributions. Beyond yielding an optimal transport plan, OT also induces a natural metric on the space of probability measures, the Wasserstein distance, which provides a geometrically meaningful way to compare distributions. This distance has proven useful in a wide range of applications, including generative modeling [4, 47, 20, 32], domain adaptation [49, 15, 14, 56], and computational geometry [46, 50].

When an optimal transport map exists, its computation can be formulated as a fluid dynamics problem that minimizes kinetic energy, as introduced by Benamou and Brenier [6]. This dynamic formulation has deepened our understanding of Wasserstein geodesics, which describes the continuous evolution of distributions along optimal transport paths. The richer information provided by this perspective not only helps the design of efficient sampling methods from high dimensional distributions [23], but also makes learning dynamical Wasserstein geodesics practically valuable in real-world settings.

In many applications – especially in machine learning and data science– only empirical samples from the underlying distributions are available, showing the need for sample-based methods (see, e.g., [20, 41, 49]). However, accurately estimating Wasserstein geodesics

Date: February 26, 2026.

2020 Mathematics Subject Classification. 93E20, 49Q22.

Key words and phrases. Wasserstein geodesics, optimal transport, neural networks, data-driven methods.

Department of Statistics, Iowa State University, Ames, IA 50011, USA.

Department of Mathematics, Iowa State University, Ames, IA 50011, USA.

and associated transport maps from finite samples remains a major challenge, especially in high-dimensional settings. Despite the recent progress in sampled-based optimal transport methods, several fundamental issues such as interpolation accuracy, computational efficiency, and scalability continue to be actively investigated. The main objective of this article is to develop a sample-based learning framework using a Lagrangian description of dynamical OT to compute the Wasserstein geodesic between source and target distributions, along with the associated velocity field.

Below we briefly review the relevant historical developments and motivate our proposed work.

1.1. Optimal Transport. The optimal transport (OT) problem, originally formulated by Monge in 1781 [45], seeks the optimal strategy to relocate the mass from a source distribution to a target distribution while minimizing the transportation cost. Specifically, given two nonnegative measures μ_a and μ_b on \mathbb{R}^d having total equal mass (often assumed to be probability distributions), Monge's problem is defined as the following constrained optimization:

$$(1.1a) \quad \min_T \int_{\mathbb{R}^d} c(x, T(x)) \mu_a(dx),$$

$$(1.1b) \quad \text{subject to } T_{\#} \mu_a = \mu_b.$$

Here, $T : \mathbb{R}^d \rightarrow \mathbb{R}^d$ is a measurable transport map, and $c(x, y)$ denotes the cost of moving a unit mass from point x to point y , commonly taken to be of the form $c(x, y) = h(x - y)$ for a strongly convex function h . The constraint (1.1b) guarantees that the pushforward of μ_a under T matches the target distribution μ_b . The pushforward measure $T_{\#} \mu_a$ is defined such that for any measurable set $E \in \mathbb{R}^d$, $T_{\#} \mu_a(E) = \mu_a(T^{-1}(E))$, or equivalently, if $X \sim \mu_a$, then $T(X) \sim \mu_b$. Monge's formulation is inherently challenging since an optimal transport map may not exist under general setups, especially when μ_a is not absolutely continuous with respect to the Lebesgue measure. Furthermore, the highly nonlinear dependence of the transportation cost on the transport map T makes the constrained optimization problem difficult.

These challenges led to further developments. In 1942, Kantorovich [31] proposed a relaxed formulation where rather than seeking an explicit transport map T , a joint distribution π , called transport plan, on the product space $\mathbb{R}^d \times \mathbb{R}^d$ is considered as a broader and more tractable framework for optimal transport. Specifically, let $\Pi(\mu_a, \mu_b)$ denote the set of all joint distributions with marginals μ_a and μ_b , respectively. The Kantorovich formulation of the optimal transport problem is then given by

$$(1.2) \quad \inf_{\pi \in \Pi(\mu_a, \mu_b)} \int_{\mathbb{R}^d \times \mathbb{R}^d} c(x, y) \pi(dxdy).$$

With appropriate assumptions on the cost function $c(\cdot, \cdot)$ and the distributions μ_a and μ_b , Monge's formulation (1.1) of OT problem admits a unique optimal transport map T^* [10, 13, 54, 53]. Moreover, the corresponding optimal transport plan:

$$\pi^* := (\text{Id} \times T^*)_{\#} \mu_a$$

solves the Kantorovich problem (1.2) [25, 53]. This connection between Monge and Kantorovich formulations is fundamental in optimal transport theory and forms the basis

for many modern computational approaches [46], while applications in high dimensional setup still remain challenging.

1.2. Density Control/Stochastic Control. Monge and Kantorovich’s formulations of the optimal transport problem are inherently static, in the sense that they focus on determining the optimal allocation of mass from a source distribution to a target distribution – that is, they address the question of “what goes where”, but not “how to get there”. However, understanding the intermediate states during transportation is crucial for many applications in various domains, including reconstructing developmental trajectories in cell reprogramming [48], shape warping in computational geometry [51], and controlling swarm robotics deployment [30, 35].

This gap can be addressed by Benamou & Brenier’s dynamic formulation [6] that captures the continuous evolution of mass over time. For the quadratic cost function $c(x, y) = \|x - y\|^2$, the dynamic OT problem can be reformulated as the following variational problem:

$$(1.3a) \quad \min_{v, \rho} \int_0^S \int_{\mathbb{R}^d} L(v(x, t)) \rho(x, t) dx dt,$$

$$(1.3b) \quad \text{subject to } \frac{\partial \rho}{\partial t} = -\nabla \cdot (v\rho),$$

$$(1.3c) \quad \rho(\cdot, 0) = \rho_a(\cdot),$$

$$(1.3d) \quad \rho(\cdot, S) = \rho_b(\cdot).$$

Here, $L(v) = \|v\|^2$ is the Lagrangian associated with kinetic energy, and ρ_a, ρ_b denote the densities of source and terminal distributions μ_a and μ_b , respectively. The time-dependent velocity field $v = v(x, t)$ in problem (1.3) specifies how to steer the mass density $\rho(x, t)$ from ρ_a to ρ_b over the time interval $[0, 1]$. The constraint equation (1.3b) is the continuity equation, which ensures mass conservation and is widely used in the context of fluid dynamics. This dynamic formulation can also be interpreted in a probabilistic framework: given (1.3b) and (1.3c), ρ describes the evolution of the distribution of a random process $X(t)$ governed by the ordinary differential equation

$$(1.4) \quad \begin{aligned} \frac{dX(t)}{dt} &= v(X(t), t), \\ X(0) &\sim \rho_a. \end{aligned}$$

In this view, the OT problem becomes a special case of a deterministic control problem, where the goal is to steer the distribution of the state $X(t)$ from the source law ρ_a to the target ρ_b by optimally choosing the control vector field $v(x, t)$. Throughout the paper, we assume without loss of generality that the terminal time is $S = 1$, since any finite horizon can be rescaled to this case.

The correspondence between OT and its dynamic formulation extends beyond the quadratic cost and holds for a broader class of cost functions. Suppose the cost function c satisfies:

$$c(x(0), x(1)) = \min_{v(\cdot, t)} \int_0^1 L(v(x(t), t)) dt,$$

$$\frac{dx(t)}{dt} = v(x(t), t)$$

for some Lagrangian $L(\cdot) \in C^1(\mathbb{R}^d)$. A notable example is $L(v) = \|v\|^p$ with $p \geq 1$, which corresponds to the well-known Wasserstein- p distance [54, 53]. By (1.4) and viewing the spatial integral in (1.3a) over \mathbb{R}^d as an expectation over the random process $X(t)$, the dynamic OT problem (1.3) can be equivalently reformulated as a stochastic control problem:

$$(1.5a) \quad \min_{v \in \mathcal{V}} \int_0^1 \mathbb{E}L(v(X(t), t)) dt,$$

$$(1.5b) \quad v(X(t), t) = \frac{dX(t)}{dt},$$

$$(1.5c) \quad X(0) \sim \rho_a,$$

$$(1.5d) \quad X(1) \sim \rho_b.$$

Here, \mathcal{V} denotes the space of admissible control policies. In many data-driven scenarios, the explicit forms of ρ_a and ρ_b are unknown, and only empirical samples are available. In such cases, a key objective is to generate new samples that are consistent with the target distribution ρ_b , given samples from both ρ_a and ρ_b .

In this work, we adopt a trajectory-based characterization of the OT problem and reformulate the stochastic optimal control problem (1.5) as a saddle point optimization. The associated functions are parameterized using neural networks. Once the optimization converges, we move forward to the second phase, where the optimal velocity field is recovered through a supervised learning problem.

The main contributions of this work are as follows:

- We propose a learning framework to estimate the optimal map, optimal velocity field, Wasserstein distance and geodesic between two distributions given only through samples. We also prove the consistency of the corresponding saddle point formulation.
- The algorithm naturally extends to general Lagrangian functions $L(v, x, t)$, including those relevant to Wasserstein- p distances. Importantly, it avoids the need to enforce the 1-Lipschitz constraint.
- We validate the effectiveness of the proposed algorithm through extensive numerical experiments on both synthetic and real datasets, in high and low-dimensional settings, and across both classical and generalized Lagrangian formulations.

1.3. Related work. Conventional methods for numerically computing the Wasserstein distance and geodesic typically rely on domain discretization, which is often mesh-dependent [8, 24, 38]. Although effective in low-dimensional settings, these approaches become computationally intractable as dimensionality increases – so called the curse of dimensionality that frequently arises in real-world applications. A common strategy for handling high-dimensional settings is to apply entropic regularization to OT [7, 16], which allows the problem to be efficiently solved using the Sinkhorn algorithm [1]. However, the Sinkhorn algorithm faces challenges when dealing with measures supported on continuous domains

or with large number of samples [26] – scenarios frequently encountered in machine learning applications.

Neural networks, renowned for their capability to approximate continuous functions [5, 17, 19], have been widely used in continuous OT algorithms to estimate transport maps. This approach enables to scale OT to high-dimensional problems that are otherwise intractable for traditional discrete methods. A major application of OT in this context is generative modeling – the task of learning models that can generate new data samples resembling a given dataset. One of the most influential frameworks in this area is the Generative Adversarial Network (GAN) [27], which formulates the learning process as a min-max game between two neural networks: a generator and a discriminator. A notable extension is the Wasserstein GAN (WGAN) [4], which incorporates OT theory by replacing the original GAN loss with the Wasserstein-1 distance, resulting in improved training stability and sample quality. However, enforcing the necessary 1-Lipschitz constraint on the discriminator has proven to be a significant challenge [29], prompting the immediate extensions and regularization strategies aimed at improving WGAN’s performance [29, 44, 55, 18]. Concurrently, several works (e.g., [11, 39, 40]) have sought to address the training instabilities in WGAN and to generalize the OT framework to more broader applications within generative modeling.

Beyond GAN-based approaches, neural networks have also been employed to learn OT maps or transportation plans from finite samples. Some methods directly parameterize the OT map T as defined in the Monge formulation (1.1) (e.g., [20, 56, 37]), while others model the stochastic transport plan π in the relaxed Kantorovich formulation (1.2) (e.g. [34, 49, 42]), which is more general since a deterministic map T may not exist in all cases. When an optimal map does exist, additional techniques such as regularization [33, 49], or cycle-consistency constraints [42] are often necessary to guide learning from transportation plans toward a well-defined and possibly unique solution. For the special case of a quadratic cost, an optimal transport map T exists under the further assumption that the source distribution is absolutely continuous [10]. In this setting, the map can be expressed as the gradient of a convex function, known as the Kantorovich potential. This insight has motivated approaches that learn these potentials using input-convex neural networks (ICNNs) [2], leading to an active line of work in this direction (e.g., [43, 21, 32]). However, most of these methods are static, focusing on solving single-shot OT problems between two fixed distributions, without modeling the interpolation path or the dynamics of the transportation process.

In contrast, our method builds upon the dynamic Benamou–Brenier (BB) formulation (1.3), which recasts OT as a fluid-flow problem and can be naturally framed as a saddle point optimization problem. The optimality conditions of the BB dynamic formulation, in both the primal and dual spaces, are characterized by a coupled PDE system or their weak formulations, as explored in [41] and [28]. Instead of solving the coupled PDE system directly, [41] took advantage of the strict convexity of the Lagrangian $L(v)$ to propose a bidirectional learning framework, demonstrating scalability to high-dimensional settings. Meanwhile [28] introduced GeONet, a mesh-invariant neural operator that learns nonlinear mapping from endpoint distributions to the entire geodesic under the classical quadratic cost by training against the coupled PDE system.

In contrast to these approaches, our framework tackles the saddle point problem directly from a stochastic optimization perspective, making it naturally compatible with general Lagrangians that may depend on the velocity field, time, and trajectory history.

1.4. Organization. The paper is organized as follows. Section 1 reviews related work in optimal transport and density control. In Sections 2 and 3, we present the formulation of our approach and address theoretical issues, including consistency. In Section 4, we validate our method through numerical experiments on both synthetic and realistic datasets. Finally, Section 5 offers concluding discussions and future directions.

2. METHOD

In this and next section, we present a data-driven framework for learning the optimal velocity field v in equation (1.5), given samples $Z \sim \rho_a$ and $Y \sim \rho_b$. The approach involves two main phases.

In the first phase, we focus on finding the optimal transport map and determining the particle trajectory $X(t)$. This is formulated as a saddle-point problem for the original task. We approximate the transport map using a parameterized deep neural network. Using this learned transport map, we derive an estimate of the velocity along the trajectory. However, this estimation only provides partial information, as our goal is to recover the full velocity field.

The second phase, described in Section 3, builds on this trajectory-based velocity estimate from the first phase to learn the complete velocity field.

We begin by describing the first phase in detail.

2.1. Trajectory characterization. To satisfy the initial state constraint in (1.5c), we reparameterize the trajectory $X(t)$ as

$$X(t) = G(t; Z) := Z + tF(Z, t), \quad 0 \leq t \leq 1,$$

where $F : \mathbb{R}^d \times [0, 1] \rightarrow \mathbb{R}^d$ is a function to be learned. This formulation ensures that the initial condition

$$X(0) = G(0; Z) = Z \sim \rho_a$$

is satisfied by construction. Here, the function G is fully and explicitly determined by F , which becomes the primary function of learning.

Along the trajectory $X(t) = G(t; Z)$, the corresponding velocity field is given by the time derivative

$$v(X(t), t) = \frac{dG(t; Z)}{dt}.$$

Based on this formulation, we define the following constrained optimization problem, which corresponds to problem (1.5).

$$(2.1a) \quad \inf_F \int_0^1 \mathbb{E} L \left(\frac{dG(t; Z)}{dt} \right) dt,$$

$$(2.1b) \quad \text{subject to } G(1; Z) \sim \rho_b,$$

$$(2.1c) \quad G(t; Z) = Z + tF(Z, t).$$

To enforce the constraint (2.1b), we evaluate the discrepancy between the target distribution ρ_b and the distribution of the particles mapped by $G(1; Z)$. A common choice for the metric is the Wasserstein-1 distance, $W(\cdot, \cdot)$, which quantifies the minimal transport cost between two probability measures. Notably, $W(\rho_1, \rho_2) = 0$ if and only if $\rho_1 = \rho_2$ almost everywhere. By replacing the terminal constraint (2.1b) with the condition

$$W(\rho_b, G(1; \cdot)_{\#}\rho_a) = 0,$$

where $G(1; \cdot)_{\#}\rho_a$ denotes the pushforward of ρ_a under $G(1; \cdot)$, we obtain an equivalent formulation of the optimization problem:

$$(2.2) \quad \inf_F \int_0^1 \mathbb{E} L \left(\frac{dG(t; Z)}{dt} \right) dt, \\ \text{subject to } W(\rho_b, G(1; \cdot)_{\#}\rho_a) = 0, \\ G(t; Z) = Z + tF(Z, t).$$

A common strategy for solving such constrained optimization problems is to introduce a Lagrange multiplier λ and reformulate the problem as a saddle-point optimization:

$$(2.3) \quad \sup_{\lambda} \inf_F \int_0^1 \mathbb{E} L \left(\frac{dG(t; Z)}{dt} \right) dt + \lambda W(\rho_b, G(1; \cdot)_{\#}\rho_a), \\ \text{subject to } G(t; Z) = Z + tF(Z, t).$$

Remark 2.1. In the Wasserstein geodesic formulation, $F(Z, t)$ can be chosen to be t -independent in cases where L does not explicitly depend on x and is solely a convex function of v , such as $L(v) = \frac{1}{2}\|v\|^2$. This choice is expected to simplify both the algorithm and learning procedure. In this work, we aim to also handle the general case with $L = L(v, x, t)$, for which $F = F(Z, t)$ is necessary. The general case will be further discussed later in Section 3.2.

2.2. Kantorovich-Rubinstein Duality. Since we only have access to samples, directly computing the Wasserstein distance $W(\cdot, \cdot)$ in the objective function (2.3) is intractable. To overcome this, we leverage Kantorovich-Rubinstein Duality [53], which gives a sample-based formulation of the Wasserstein-1 distance.

Let $\hat{Y} := G(1; Z)$ denote a random sample from the pushforward distribution $G(1; \cdot)_{\#}\rho_a$. Then, the Wasserstein-1 distance $W(\rho_b, G(1; \cdot)_{\#}\rho_a)$ can then be expressed as:

$$(2.4) \quad W(\rho_b, G(1; \cdot)_{\#}\rho_a) = \sup_{\phi: 1\text{-Lip}} \mathbb{E} [\phi(\hat{Y})] - \mathbb{E} [\phi(Y)] = \sup_{\phi: 1\text{-Lip}} \mathbb{E} [\phi(G(1; Z))] - \mathbb{E} [\phi(Y)],$$

where the supremum is taken over all 1-Lipschitz functions ϕ .

To further simplify the formulation, we introduce a random variable U uniformly distributed in $[0, 1]$, independent of Z and Y . Incorporating this into the saddle-point problem, we rewrite the objective:

$$\sup_{\lambda} \inf_F \int_0^1 \mathbb{E} L \left(\frac{dG(t; Z)}{dt} \right) dt + \lambda W(\rho_b, G(1; \cdot)_{\#}\rho_a)$$

as

$$\sup_{\lambda} \inf_F \mathbb{E}_{Z \sim \rho_a, U \sim U(0,1)} \left[L \left(\frac{dG(U; Z)}{dt} \right) \right] + \lambda \sup_{\phi:1\text{-Lip}} (\mathbb{E} [\phi(G(1; Z))] - \mathbb{E} [\phi(Y)]).$$

Assuming the order of optimization can be exchanged, we arrive at the following saddle-point formulation:

$$(2.5) \quad \inf_F \sup_{\lambda} \sup_{\phi:1\text{-Lip}} \mathbb{E} \left[L \left(\frac{dG(U; Z)}{dt} \right) \right] + \lambda (\mathbb{E} [\phi(G(1; Z))] - \mathbb{E} [\phi(Y)]).$$

Finally, by absorbing the scalar Lagrangian multiplier λ into the 1-Lipschitz function ϕ , we obtain a more streamlined formulation in which ϕ is treated as a general Lipschitz function. This leads to the following min-max problem:

$$(2.6a) \quad \inf_F \sup_{\phi:\text{Lip}} \mathbb{E} \left[L \left(\frac{dG(U; Z)}{dt} \right) \right] + (\mathbb{E} [\phi(G(1; Z))] - \mathbb{E} [\phi(Y)]),$$

$$(2.6b) \quad \text{subject to } G(t; Z) = Z + tF(Z, t).$$

The following result guarantees the theoretical consistency of this formulation.

Theorem 2.2. *Suppose the min-max problem (2.6) admits a unique solution (F^*, ϕ^*) . Then F^* is also a solution to problem (2.2), which is equivalent to the original problem (2.1).*

The proof is given in Appendix A.

In practical implementations, the expectations in (2.6) typically do not admit closed-form expressions. Nevertheless, by the law of large numbers, these expectations can be approximated to arbitrary accuracy using sample means, provided that enough independent samples are available.

2.3. Deep neural network approximations. To numerically solve the optimization problem (2.6), we approximate the functions F and ϕ using deep neural networks.

A fully connected feedforward neural network can be mathematically expressed as a composition of linear transformations and nonlinear activation functions. Specifically, a neural network $f_{\theta} : \mathbb{R}^{N_1} \rightarrow \mathbb{R}^{N_L}$ of depth $L - 2$ is defined as

$$f_{\theta}(\cdot) := h_{L-1} \circ \sigma_{L-2} \circ h_{L-2} \circ \cdots \circ \sigma_1 \circ h_1,$$

where each $h_j : \mathbb{R}^{N_j} \rightarrow \mathbb{R}^{N_{j+1}}$, $j = 1, 2, \dots, L - 1$ is a linear transformation of the form

$$h_j(x) = W_j x + b_j,$$

with weight matrix $W_j \in \mathbb{R}^{N_{j+1} \times N_j}$ and bias vectors $b_j \in \mathbb{R}^{N_{j+1}}$. The function $\sigma_j : \mathbb{R} \rightarrow \mathbb{R}$ is a nonlinear activation function applied component-wise to the output of h_j . The set of all trainable parameters in the network is represented by $\theta \in \mathbb{R}^N$, which includes all weights and biases: $W_1, b_1, \dots, W_{L-1}, b_{L-1}$, with

$$N = \sum_{j=1}^{L-1} (N_j + 1) N_{j+1}.$$

Common activation functions include the hyperbolic tangent (tanh), sigmoid, rectified linear unit (ReLU) and Leaky ReLU (LReLU) [3]. In our setting, we use two deep neural networks $F_\theta : \mathbb{R}^d \rightarrow \mathbb{R}^d$ and $\phi_\omega : \mathbb{R}^d \rightarrow \mathbb{R}$, parameterized by θ and ω , respectively, to approximate F and ϕ . We select $L = 5$ for both F_θ and ϕ_ω . For the activation function σ_j in F_θ and ϕ_ω , we choose Leaky ReLU function with negative slope 0.2 throughout the experiments in Section 4. The formulation of this Leaky ReLU is

$$\text{LReLU}(x) = \begin{cases} x, & \text{if } x \geq 0 \\ 0.2x, & \text{otherwise.} \end{cases}$$

Given independent samples $\{Z_i\}_{i=1}^n \sim \rho_a$ and $\{Y_i\}_{i=1}^n \sim \rho_b$, we discretize and approximate the objective in problem (2.6) using empirical averages. Specifically, with $\{U_j\}_{j=1}^m$ as independent samples drawn from $U(0, 1)$, we propose the following finite-sample formulation (2.7)

$$\min_{\theta} \max_{\omega} \frac{1}{nm} \sum_{j=1}^m \sum_{i=1}^n \left[L \left(\frac{dG_\theta(U_j; Z_i)}{dt} \right) \right] + \left(\frac{1}{n} \sum_{i=1}^n [\phi_\omega(G_\theta(1; Z_i))] - \frac{1}{n} \sum_{i=1}^n [\phi_\omega(Y_i)] \right),$$

subject to $G_\theta(t; Z_i) = Z_i + tF_\theta(Z_i, t)$.

The proposed algorithm for solving this min-max problem is provided in Algorithm 1.

Remark 2.3. In fact, implementing the algorithm does not require the sample sets drawn from the two distributions ρ_a and ρ_b to have the same size, nor does it require the samples to be paired. This is because the second term in (2.7), where the terminal constraint is enforced weakly, independently approximates the expectations with respect to each distribution. This observation also applies to Algorithm 1 presented later.

2.4. Lipschitz constraint on the critic neural network. Our learning problem (2.7) falls within the framework of Generative Adversarial Networks (GANs) [27], where the actor network (F_θ) and the critic network (ϕ_ω) are adversarially trained. A key distinction in our setup is the application of a Lipschitz constraint on the critic function in (2.6a), derived from the use of the Wasserstein-1 distance. Importantly, our framework enforces a general Lipschitz constraint, rather than the stricter 1-Lipschitz condition commonly seen in Wasserstein GANs [4]. Many subsequent works [2, 32, 21, 43] have addressed the challenges posed by enforcing this non-trivial constraint. To implement the Lipschitz condition in our parameterized critic network, we follow the approach in [44], applying spectral normalization to each weight matrix \tilde{W}_j of ϕ_ω , and selecting 1-Lipschitz activation functions σ_j . This ensures that the resulting network is 1-Lipchitz. We then scale the output by a learnable parameter, inspired by the derivation of our method between (2.5) and (2.6), to generalize beyond the 1-Lipschitz case.

Finally, the critic network ϕ_ω is defined as

$$\phi_\omega(\cdot) := \lambda \cdot \tilde{h}_{m-1} \circ \sigma_{m-2} \circ \tilde{h}_{m-2} \circ \cdots \circ \sigma_1 \circ \tilde{h}_1,$$

where each transformed layer $\tilde{h}_j(x) = (\tilde{W}_j x + b_j) / \|\tilde{W}_j\|_2$, and $\|\tilde{W}_j\|_2$ is the spectral norm of \tilde{W}_j . Again, Leaky ReLU with negative slope 0.2 is used as the activation throughout the experiments in Section 4.

3. VELOCITY FIELD RECOVERY

3.1. Velocity field recovery. Keep in mind that in problem (1.5), a key objective is to recover the full velocity field $v(x, t)$ – meaning we seek to determine the value of the vector field at any location $x \in \mathbb{R}^d$ and time $t \in [0, 1]$. However, the learning framework proposed for problem (2.6) does not directly yield an explicit representation of $v(x, t)$.

To illustrate this, let F_{θ^*} denote the numerical solution to problem (2.6). The estimated trajectory $G_{\theta^*}(t; z)$ starting at $z \in \mathbb{R}^d$ is given by

$$G_{\theta^*}(t; z) := z + tF_{\theta^*}(z, t).$$

Using this learned trajectory G_{θ^*} and equation (1.5b), we can estimate the velocity along the trajectory as

$$v_{\theta^*}(G_{\theta^*}(t; z), t) := \frac{dG_{\theta^*}(t; z)}{dt}.$$

However, this only provides the values of the velocity along trajectories, not the full velocity field $v(x, t)$ where x and t are independent.

To recover the complete velocity field $v(x, t)$, where the spatial and temporal arguments are independent, we introduce another neural network v_η to approximate the true time-varying velocity field. We treat $v_{\theta^*}(G_{\theta^*}(U; Z), U)$ as samples from the ground truth and train v_η using supervised learning.

By employing the squared error loss, we formulate the following optimization problem to learn the velocity field v for problem (1.5):

$$(3.1) \quad \min_{\eta} \frac{1}{mn} \sum_{j=1}^m \sum_{i=1}^n \left\| v_\eta(G_{\theta^*}(U_j; Z_i), U_j) - \frac{dG_{\theta^*}(U_j; Z_i)}{dt} \right\|^2.$$

As our Phase 2, this procedure is described in Algorithm 2.

Remark 3.1. Regarding the samples Z_i and U_j used for training in Phase 2, we recommend drawing fresh samples rather than reusing those from Phase 1. This helps prevent Phase 2 from simply memorizing velocities along the specific trajectories learned in Phase 1. In the synthetic experiments presented in Section 4, where the true velocity field v^* is available, we observe no significant difference in the error between v_η and v^* when comparing fresh samples to reused Phase 1 samples. However, this may be due to the relative simplicity of the synthetic settings, which makes the velocity field easier to learn. Moreover, since the trajectories learned in Phase 1 are treated as "ground truth" during supervised training in Phase 2, a zero Phase 2 loss does not guarantee convergence of v_η to v^* (see Appendix B for more details).

In summary, the proposed framework addresses problem (1.5) in two phases: first by solving (2.7) to estimate the geodesic, and then by solving (3.1) to learn the full velocity field. It is worth noting that in some applications, the objective is to generate additional samples from ρ_b , interpolate intermediate trajectories, or estimate velocities along the transport paths. In such cases, implementing Phase 1 to obtain the transport map is already sufficient, and Phase 2 – aimed at recovering the Euler velocity field – is not necessary.

3.2. Extension to general Lagrangian. Our method extends naturally to time-dependent optimal transport problems, in which the transportation cost also depends on the transport trajectory, rather than just the initial and terminal points. In such settings, a typical Lagrangian takes the form

$$L(x, v, t) = \frac{\|v\|^2}{2} - V(x),$$

where $V : \mathbb{R}^d \rightarrow \mathbb{R}$ is a potential function [53]. For a general Lagrangian, the existence and uniqueness of an optimal solution are guaranteed when $L(x, v, t)$ is strictly convex and superlinear in the velocity variable v [12, 53, 22, 9]. For further details about the time-dependent optimal transport, we refer the reader to Villani [53] and Chen et al. [12]. The Lagrangian in our previous setup (1.5) is a special case of this more general formulation: by selecting $V(x) = 0$, we recover the simpler form $L(x, v, t) = L(v) = \frac{\|v\|^2}{2}$. Using a similar approach to that in Section 2, we can numerically solve the more general version of the dynamical optimal transport problem:

$$\begin{aligned} \min_v \int_0^1 \mathbb{E} L\left(X(t), v(X(t), t), t\right) dt, \\ v(X(t), t) = \frac{dX(t)}{dt}, \\ X(0) \sim \rho_a, \\ X(1) \sim \rho_b. \end{aligned}$$

In practice, we implement this by replacing the simple kinetic energy with the more general Lagrangian:

$$L\left(G_\theta(U_j; Z_i), \frac{dG_\theta(U_j; Z_i)}{dt}, U_j\right)$$

for the corresponding term in (2.7) and Algorithm 1. A numerical experiment in this general setting will be given in Section 4. It is worth noting that many existing methods based on the Benamou–Brenier dynamical formulation (e.g., [41, 28]) primarily focus on the setting where $L = L(v)$ depends solely on v and is strictly convex. In such case, the associated Hamiltonian $H(p) := \sup_v v \cdot p - L(v)$ admits an explicit form. In contrast, our framework naturally extends to the more general class of Lagrangian considered above.

4. NUMERICAL EXPERIMENTS

In this section, we evaluate our algorithms on both synthetic and real datasets. The neural networks used for the transport map G_θ , the critic ϕ_ω , and the velocity field v_η each consists of three hidden layers and are trained using RMSprop optimizer [52]. We adopt the Leaky ReLU activation function with a negative slope of 0.2 across all experiments.

Except for the general Lagrangian case in Synthetic-4, we use the standard quadratic Lagrangian $L(v) = \|v\|^2$. Under this choice, the first term in the objective function (2.7) serves as an estimate of the squared Wasserstein-2 distance between the source and target distributions.

For the random variable $\{U_j\}_{j=1}^m$ used in Algorithm 1 and 2, we adopt $m = 10$ equally spaced time steps from $t = 0.1$ to $t = 1.0$ in Synthetic-1 through Synthetic-3. We

Algorithm 1 Training Procedure for Solving Problem (2.7).

-
- 1: **Input:** Sample size n ; number of time samples m ; Lagrangian $L(v)$.
 - 2: Initialize networks F_θ and ϕ_ω . Define $G_\theta(t; z) := z + tF_\theta(z, t)$ for $(z, t) \in \mathbb{R}^d \times [0, 1]$.
 - 3: **while** θ has not converged **do**
 - 4: Sample $\{Z_i\}_{i=1}^n \stackrel{\text{i.i.d.}}{\sim} \rho_a$ and $\{Y_i\}_{i=1}^n \stackrel{\text{i.i.d.}}{\sim} \rho_b$.
 - 5: Compute the objective function for ϕ_ω

$$\ell_\omega \leftarrow \frac{1}{n} \sum_{i=1}^n [\phi_\omega(G_\theta(1; Z_i))] - \frac{1}{n} \sum_{i=1}^n [\phi_\omega(Y_i)].$$

- 6: Update ω by ascending ℓ_ω .
- 7: Sample $\{Z_i\}_{i=1}^n \stackrel{\text{i.i.d.}}{\sim} \rho_a$ and $\{U_j\}_{j=1}^m \stackrel{\text{i.i.d.}}{\sim} U(0, 1)$.
- 8: Compute the objective function for F_θ

$$\ell_\theta \leftarrow \frac{1}{mn} \sum_{j=1}^m \sum_{i=1}^n L\left(\frac{dG_\theta(U_j; Z_i)}{dt}\right) + \frac{1}{n} \sum_{i=1}^n \phi_\omega(G_\theta(1; Z_i)).$$

- 9: Update θ by descending ℓ_θ .
 - 10: **end while**
 - 11: **Output:** Trained geodesic G_θ and critic ϕ_ω .
-

Algorithm 2 Training Procedure for Solving Problem (3.1).

-
- 1: **Input:** Trained neural network G_{θ^*} from Algorithm 1.
 - 2: Initialize the network v_η .
 - 3: **while** η has not converged **do**
 - 4: Sample $\{Z_i\}_{i=1}^n \stackrel{\text{i.i.d.}}{\sim} \rho_a$ and $\{U_j\}_{j=1}^m \stackrel{\text{i.i.d.}}{\sim} U(0, 1)$.
 - 5: Compute the object function for v_η

$$\ell_\eta = \frac{1}{mn} \sum_{j=1}^m \sum_{i=1}^n \left\| v_\eta(G_{\theta^*}(U_j; Z_i), U_j) - \frac{dG_{\theta^*}(U_j; Z_i)}{dt} \right\|_2^2.$$

- 6: Update v_η by descending ℓ_η .
 - 7: **end while**
 - 8: **Output:** Trained velocity field v_η .
-

set $m = 20$ in Synthetic-4 and in the Real Data case. In Synthetic-1 and Synthetic-3 where the analytical velocity field v^* are available, we compare v^* with the learned v_η in the Appendix B. For the real data scenario, we apply our algorithm to the MNIST handwritten digits dataset [36], which serves as a high-dimensional benchmark. The velocity fields reported in this section are trained with fresh samples Z_i and U_j . That is, new samples are drawn for the supervised training in Phase 2.

Synthetic Experiments

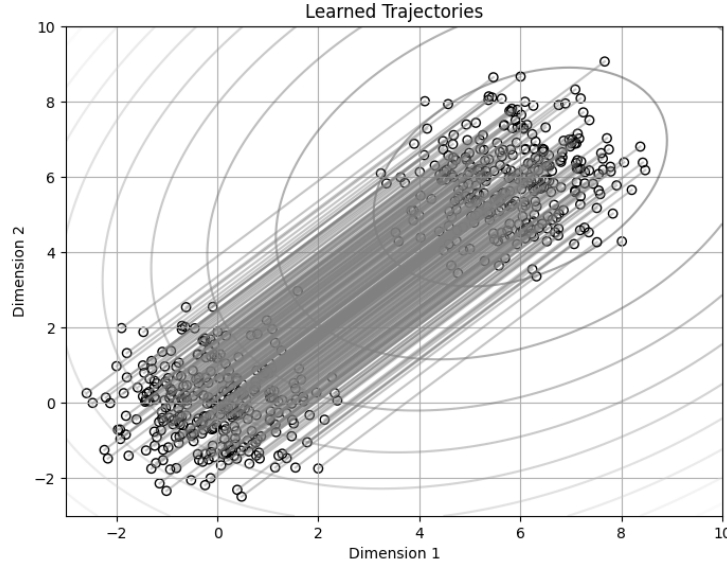


FIGURE 1. Phase 1 of Synthetic-1: Samples of the source distribution ρ_a (open circle at the bottom left corner) are transported to the upper right corner. Each gray line illustrates the learned trajectory $G_\theta(t; \cdot)_{\# \rho_a}$. The contour shows the true log density of ρ_b .

Synthetic-1: 2D-Gaussian. In this 2D example, both ρ_a and ρ_b are Gaussian distributions

$$\rho_a = \mathcal{N} \left(\begin{pmatrix} 0 \\ 0 \end{pmatrix}, \begin{bmatrix} 1 & 0 \\ 0 & 1 \end{bmatrix} \right), \quad \rho_b = \mathcal{N} \left(\begin{pmatrix} 6 \\ 6 \end{pmatrix}, \begin{bmatrix} 1.5 & 0.5 \\ 0.5 & 1.5 \end{bmatrix} \right).$$

Figure 1 shows the learned trajectories of samples of ρ_a in Phase 1. Figure 2 presents the learned velocity field at selected time points in Phase 2.

Synthetic-2: Mixture of 2D-Gaussians. Here, ρ_a is a standard 2-dimensional Gaussian, and ρ_b is a mixture of 4 Gaussian components with the same covariance matrix as ρ_a , positioned at the corners of a square. Figure 3 and 4 present the learned geodesic and velocity field.

Synthetic-3: 10D-Gaussians. For this experiment in the 10-dimensional space, ρ_a is chosen to be a standard Gaussian and ρ_b another Gaussian. The learned geodesic and velocity field projected to the 2-dimensional space are shown in Figure 5 and 6, respectively.

Synthetic-4: 2D Harmonic Oscillation with general Lagrangian. In this example, we consider the 2-dimensional harmonic oscillation. Specifically, for $x = (x_1, x_2)$ and v in \mathbb{R}^2 , consider the Lagrangian

$$L(x, v) = \frac{1}{2} (\|v\|^2 - \omega_1^2 x_1^2 - \omega_2^2 x_2^2),$$

where $\omega_1, \omega_2 > 0$ are given. Solve the optimization problem:

$$\min_v \frac{1}{2} \int_0^1 \mathbb{E} [\|v(X(t), t)\|^2 - \omega_1^2 X_1^2(t) - \omega_2^2 X_2^2(t)],$$

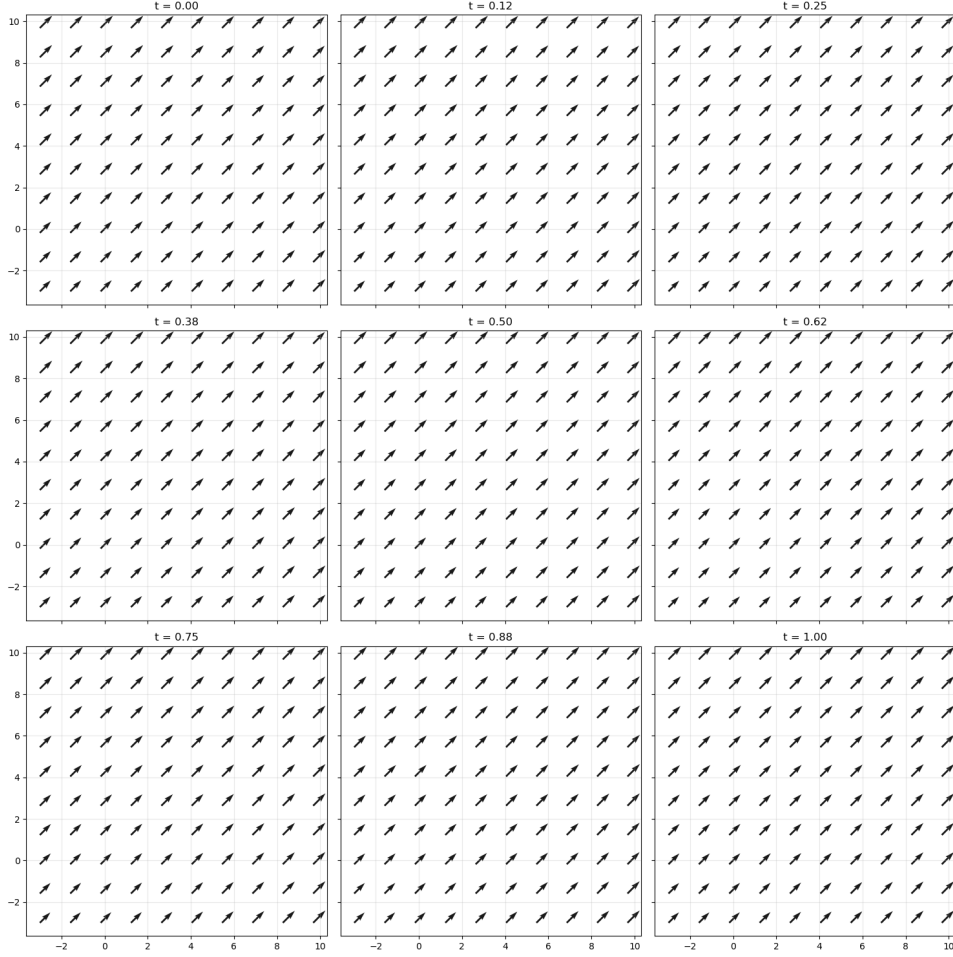


FIGURE 2. Phase 2 of Synthetic-1: learned velocity fields at selected time points. The arrows illustrate the direction and magnitude of the learned velocity.

$$v(X(t), t) = \frac{dX(t)}{dt},$$

$$X(0) \sim \rho_a, \quad X(1) \sim \rho_b.$$

We consider the case $\omega_1 = 1.2, \omega_2 = 0.1$ and the source and target distributions are defined as

$$\rho_a = \mathcal{N}\left(\begin{pmatrix} m_{a,1} \\ m_{a,2} \end{pmatrix}, \begin{bmatrix} 0.01 & 0 \\ 0 & 0.01 \end{bmatrix}\right), \quad \rho_b = \mathcal{N}\left(\begin{pmatrix} m_{b,1} \\ m_{b,2} \end{pmatrix}, \begin{bmatrix} 0.01 & 0 \\ 0 & 0.01 \end{bmatrix}\right),$$

where $m_{a,1} = m_{a,2} = 3, m_{b,1} = m_{b,2} = 5$. In this setting, the analytical solution $X(t)$ is available

$$(4.1) \quad \begin{aligned} X_1(t; x) &= \frac{\sin(\omega_1(1-t)) + \sin(\omega_1 t)}{\sin \omega_1} x_1 + \frac{\sin(\omega_1 t)}{\sin \omega_1} (m_{b,1} - m_{a,1}) \\ X_2(t; x) &= \frac{\sin(\omega_2(1-t)) + \sin(\omega_2 t)}{\sin \omega_2} x_2 + \frac{\sin(\omega_2 t)}{\sin \omega_2} (m_{b,2} - m_{a,2}) \end{aligned}$$

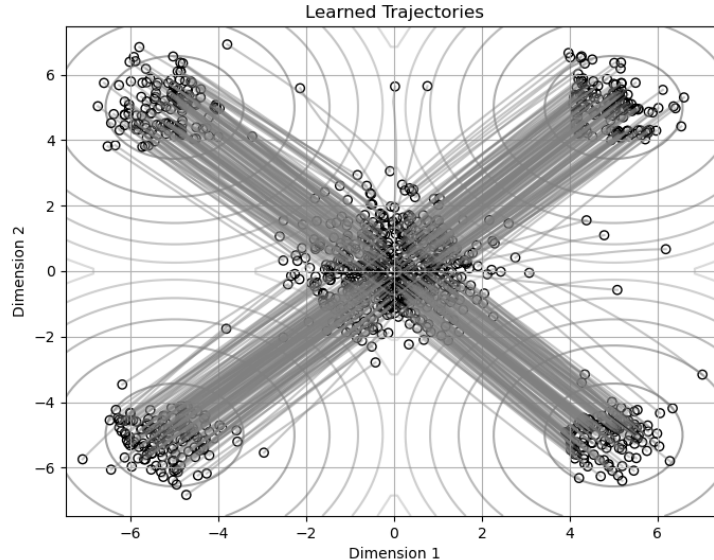


FIGURE 3. Phase 1 of Synthetic-2: Samples of the source distribution ρ_a (open circle at the center) are transported to the four corners. Each gray line illustrates the learned trajectory $G_\theta(t; \cdot)_{\# \rho_a}$. The contour shows the true log density of ρ_b .

This analytical trajectory and the learned geodesic in Phase 1 are shown in Figure 7. In Figure 8, the velocity field learned in Phase 2 is shown.

Real Data: MNIST digit transformation. As a high-dimensional example (28×28 dimensions), we consider the MNIST dataset. Specifically, we aim to learn a transport map from digit 6 (representing ρ_a) to digit 9 (representing ρ_b). Figure 9 and 10 illustrate the learned geodesic trajectory in Phase 1.

Comment on the results of the numerical experiments. We observed that the generated samples $G(1; \cdot)_{\# \rho_a}$ exhibit patterns similar to the target distribution ρ_b , as evidenced by comparing the empirical distribution of the pushed open circle to the true log density contour in synthetic cases, and by the convergence of the Wasserstein-1 distance toward zero during Phase 1 training in most cases (see Appendix B for details during training). Furthermore, visualization of particle trajectories suggest that the transport of samples occurs efficiently. However, we note that the objective function values often fluctuate during Phase 1 training, which may be due to the inherent instability of optimizing a min-max problem involving two adversarial networks. In some cases (e.g., Figure 3 of Synthetic-2), the mapped distribution does not fully match the target distribution, as indicated by the failure of the estimated Wasserstein-1 distance to converge to zero. We acknowledge the existence of additional regularization techniques for the critic function (e.g., [29]) that might improve target distribution matching in Phase 1. To address instability, alternative optimization methods may help improve performance. In addition, we observe that neural network hyperparameters – such as the choice of activation function,

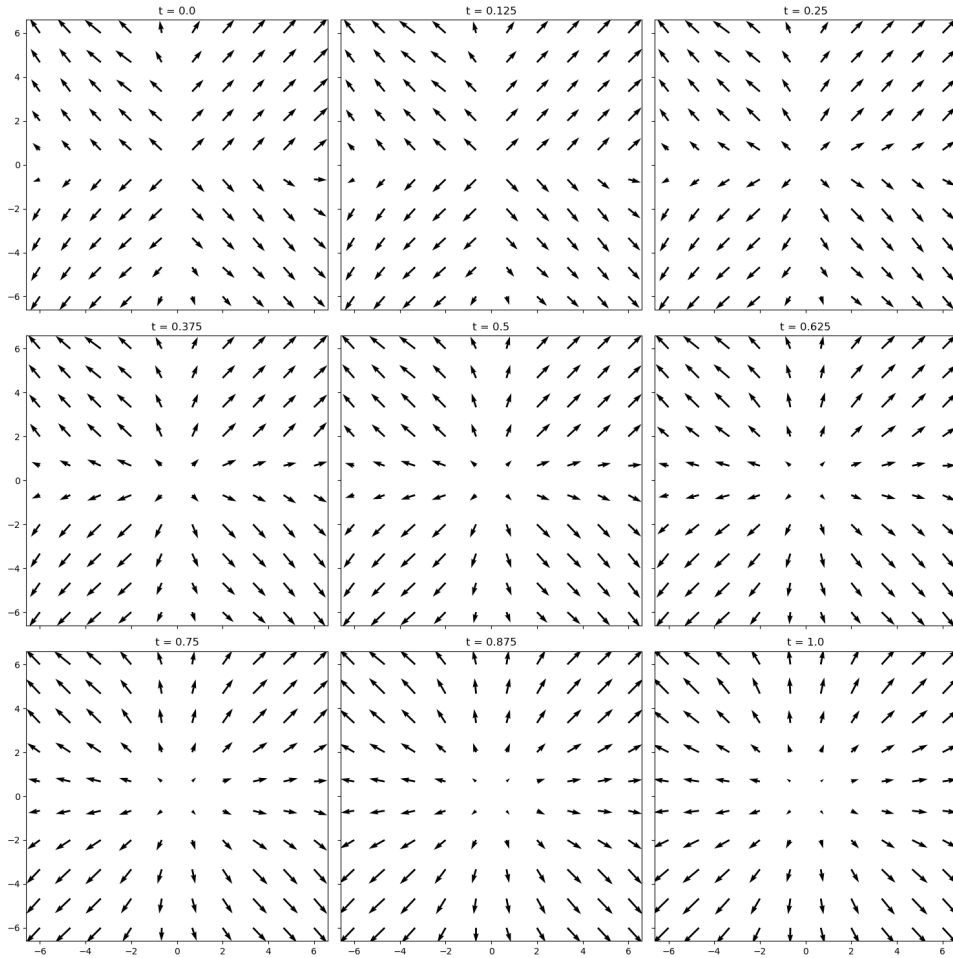


FIGURE 4. Phase 2 of Synthetic-2: learned velocity fields at selected time points. The arrows illustrate the direction and magnitude of the learned velocity.

depth, width, and learning rate – can significantly affect performance, including the quality of distribution matching. Thus, additional regularization and careful hyperparameter tuning are two practical strategies for improving performance in cases where matching the target distribution and the pushforward distribution is particularly challenging. In Phase 2, where the complete velocity field is learned, we observe that the discrepancy between the learned and the true velocity fields (e.g., Figure 16 in Appendix B) does not fully vanish. This may stem from using the Phase 1 learned trajectories as samples for ground truth, even though they are only approximations.

5. CONCLUSION

In this paper, we propose a sample-based learning framework to estimate the OT geodesic and corresponding velocity field for transporting the source distribution into the target distribution with minimum cost. Furthermore, the learning algorithm can be naturally applied to general Lagrangian where the transportation cost may depends on the velocity field, transport trajectory and time, including the classical case of simple kinetic energy.

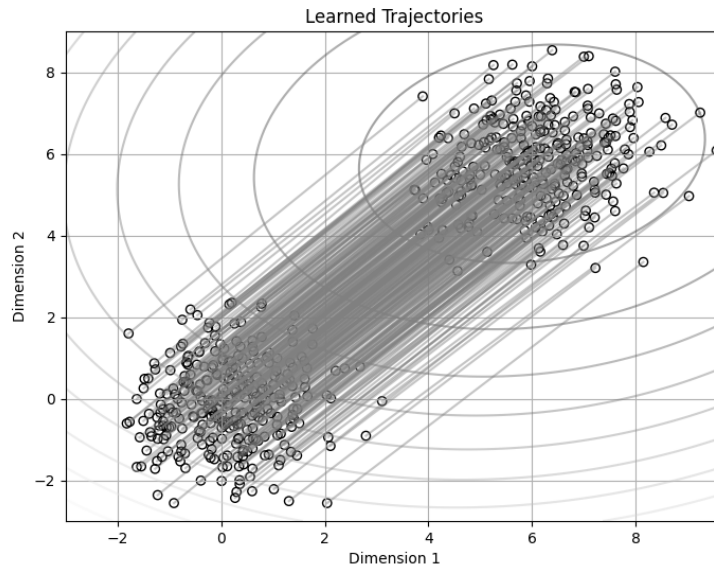


FIGURE 5. Phase 1 of Synthetic-3: 2-dimensional projection of the 10-dimensional distributions. Samples of the source distribution ρ_a (open circle at the bottom left corner) are transported to the upper right corner. Each gray line illustrates the learned trajectory $G_\theta(t; \cdot)_{\#}\rho_a$. The contour shows the true log density of ρ_b .

We demonstrate the performance of our algorithm through a series of experiments including synthetic and realistic data, high-dimensional and low-dimensional setups, classical and general Lagrangian.

DECLARATIONS

Conflict of Interest. The authors declare that they have no known competing financial interests or personal relationships that could have appeared to influence the work reported in this paper.

Data Availability. The datasets generated during the the study are available from the corresponding author on reasonable request. The MNIST dataset used is a publicly available benchmark.

REFERENCES

- [1] Jason Altschuler, Jonathan Niles-Weed, and Philippe Rigollet, *Near-linear time approximation algorithms for optimal transport via sinkhorn iteration*, Advances in Neural Information Processing Systems, vol. 30, Curran Associates, Inc., 2017.
- [2] Brandon Amos, Lei Xu, and J Zico Kolter, *Input convex neural networks*, International Conference on Machine Learning, PMLR, 2017, pp. 146–155.
- [3] Andrea Apicella, Francesco Donnarumma, Francesco Isgrò, and Roberto Prevede, *A survey on modern trainable activation functions*, Neural Networks **138** (2021), 14–32.
- [4] Martin Arjovsky, Soumith Chintala, and Léon Bottou, *Wasserstein generative adversarial networks*, International Conference on Machine Learning, PMLR, 2017, pp. 214–223.

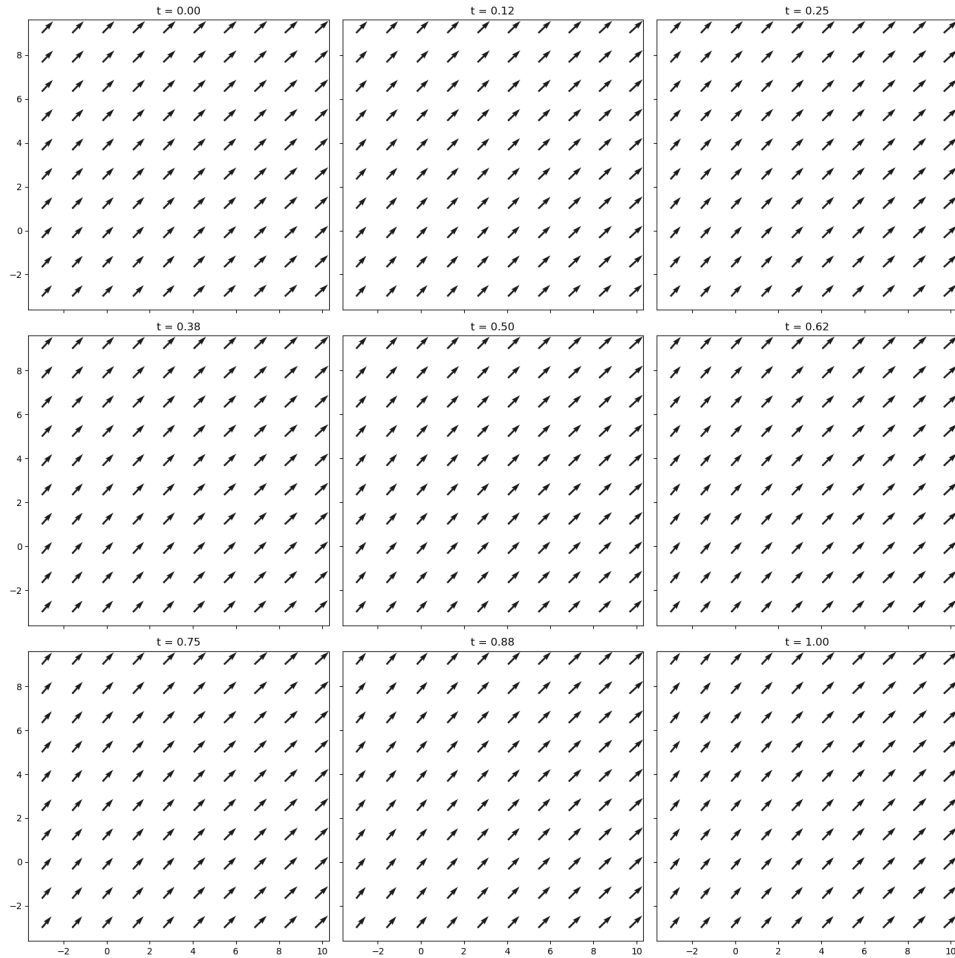


FIGURE 6. Phase 2 of Synthetic-3: learned velocity fields at selected time points. The arrows illustrate the direction and magnitude of the learned velocity.

- [5] Andrew R Barron, *Universal approximation bounds for superpositions of a sigmoidal function*, IEEE Transactions on Information theory **39** (1993), no. 3, 930–945.
- [6] Jean-David Benamou and Yann Brenier, *A computational fluid mechanics solution to the Monge-Kantorovich mass transfer problem*, Numerische Mathematik **84** (2000), no. 3, 375–393.
- [7] Jean-David Benamou, Guillaume Carlier, Marco Cuturi, Luca Nenna, and Gabriel Peyré, *Iterative Bregman projections for regularized transportation problems*, SIAM Journal on Scientific Computing **37** (2015), no. 2, A1111–A1138.
- [8] Jean-David Benamou, Brittany D Froese, and Adam M Oberman, *Two numerical methods for the elliptic Monge-Ampère equation*, ESAIM: Mathematical Modelling and Numerical Analysis **44** (2010), no. 4, 737–758.
- [9] Patrick Bernard and Boris Buffoni, *Optimal mass transportation and mather theory*, Journal of the European Mathematical Society **9** (2007), no. 1, 85–121.
- [10] Yann Brenier, *Polar factorization and monotone rearrangement of vector-valued functions*, Communications on Pure and Applied Mathematics **44** (1991), no. 4, 375–417.
- [11] Jiezhong Cao, Langyuan Mo, Yifan Zhang, Kui Jia, Chunhua Shen, and Mingkui Tan, *Multi-marginal Wasserstein GAN*, Advances in Neural Information Processing Systems **32** (2019).

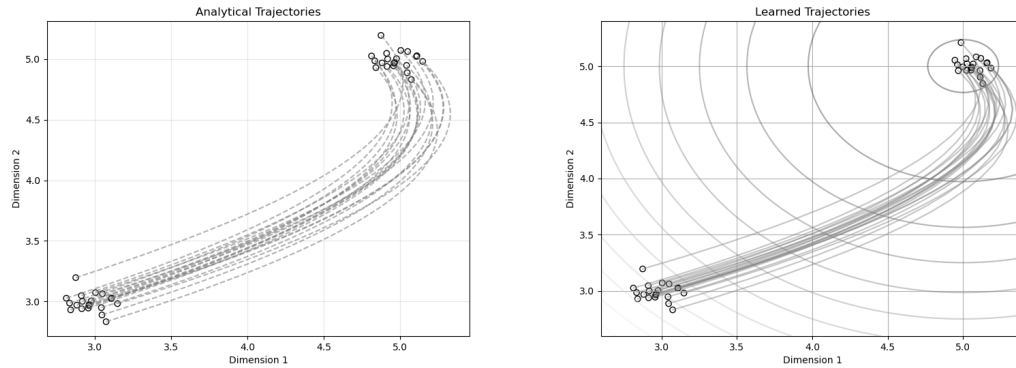


FIGURE 7. Phase 1 of Synthetic-4: Left panel presents the analytical trajectories (4.1) of 20 samples from ρ_a (open circle at the bottom left corner). In the right panel, those 20 samples are transported by the learned map, where the gray lines illustrate the learned trajectories $G_\theta(t; \cdot)_{\#}\rho_a$. The contour in the right panel shows the true log density of ρ_b .

- [12] Yongxin Chen, Tryphon T Georgiou, and Michele Pavon, *Optimal transport over a linear dynamical system*, IEEE Transactions on Automatic Control **62** (2016), no. 5, 2137–2152.
- [13] ———, *Optimal transport in systems and control*, Annual Review of Control, Robotics, and Autonomous Systems **4** (2021), no. 1, 89–113.
- [14] Nicolas Courty, Rémi Flamary, Amaury Habrard, and Alain Rakotomamonjy, *Joint distribution optimal transportation for domain adaptation*, Advances in Neural Information Processing Systems **30** (2017).
- [15] Nicolas Courty, Rémi Flamary, Devis Tuia, and Alain Rakotomamonjy, *Optimal transport for domain adaptation*, IEEE transactions on pattern analysis and machine intelligence **39** (2016), no. 9, 1853–1865.
- [16] Marco Cuturi, *Sinkhorn distances: Lightspeed computation of optimal transport*, Advances in Neural Information Processing Systems **26** (2013), 2292–2300.
- [17] George Cybenko, *Approximation by superpositions of a sigmoidal function*, Mathematics of control, signals and systems **2** (1989), no. 4, 303–314.
- [18] Nhan Dam, Quan Hoang, Trung Le, Tu Dinh Nguyen, Hung Bui, and Dinh Phung, *Three-player Wasserstein GAN via amortised duality*, Proceedings of the Twenty-Eighth International Joint Conference on Artificial Intelligence, IJCAI-19, International Joint Conferences on Artificial Intelligence Organization, 7 2019, pp. 2202–2208.
- [19] Tim De Ryck, Samuel Lanthaler, and Siddhartha Mishra, *On the approximation of functions by tanh neural networks*, Neural Networks **143** (2021), 732–750.
- [20] Jiaojiao Fan, Shu Liu, Shaojun Ma, Haomin Zhou, and Yongxin Chen, *Neural Monge map estimation and its applications*, Transactions on Machine Learning Research (2023).
- [21] Jiaojiao Fan, Amirhossein Taghvaei, and Yongxin Chen, *Scalable computations of Wasserstein barycenter via input convex neural networks*, International Conference on Machine Learning, PMLR, 2021, pp. 1571–1581.
- [22] Alessio Figalli, *Optimal transportation and action-minimizing measures*, vol. 8, Edizioni della Normale, 2008.
- [23] Chris Finlay, Jörn-Henrik Jacobsen, Levon Nurbekyan, and Adam M Oberman, *How to train your neural ode: The world of jacobian and kinetic regularization*, Proceedings of the 37th International Conference on Machine Learning (ICML), 2020.
- [24] Wilfrid Gangbo, Wuchen Li, Stanley Osher, and Michael Puthawala, *Unnormalized optimal transport*, Journal of Computational Physics **399** (2019), 108940.

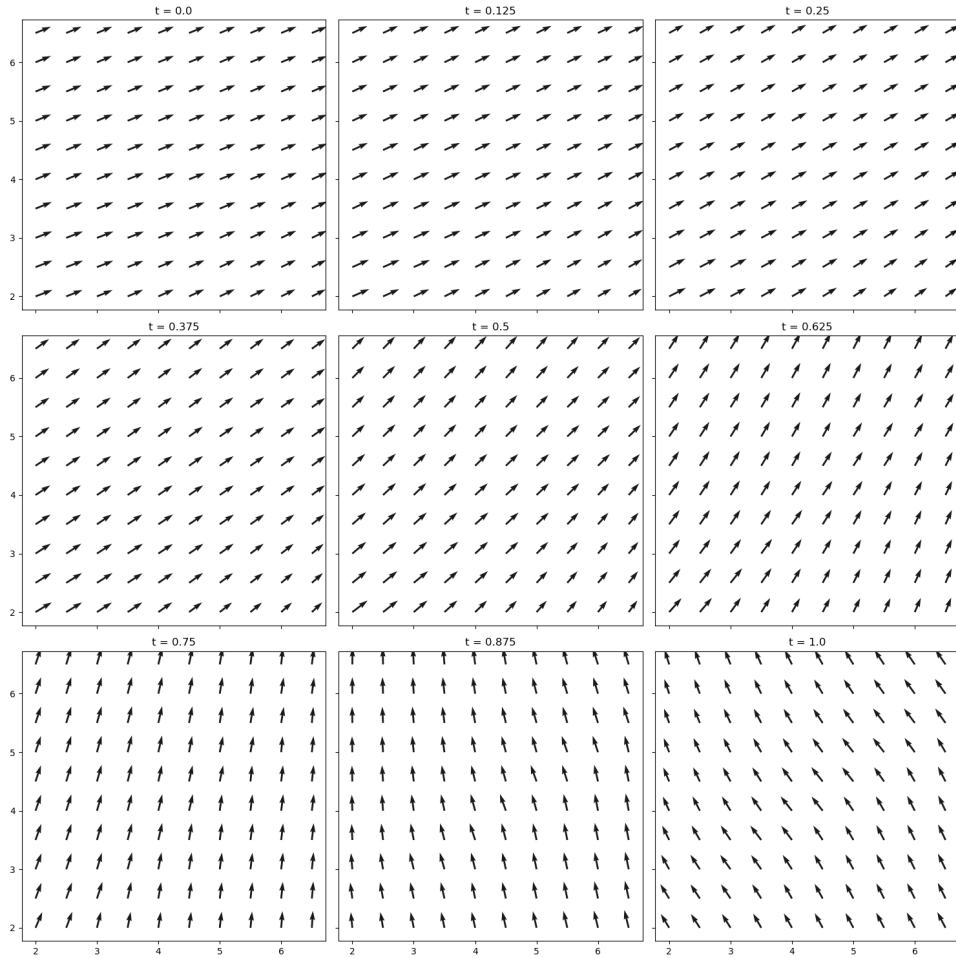


FIGURE 8. Phase 2 of Synthetic-4: learned velocity fields at selected time points. The arrows illustrate the direction and magnitude of the learned velocity.

- [25] Wilfrid Gangbo and Robert J McCann, *The geometry of optimal transportation*, *Acta Mathematica* **177** (1996), 113–161.
- [26] Aude Genevay, Marco Cuturi, Gabriel Peyré, and Francis Bach, *Stochastic optimization for large-scale optimal transport*, *Advances in Neural Information Processing Systems* **29** (2016).
- [27] Ian J Goodfellow, Jean Pouget-Abadie, Mehdi Mirza, Bing Xu, David Warde-Farley, Sherjil Ozair, Aaron Courville, and Yoshua Bengio, *Generative adversarial nets*, *Advances in Neural Information Processing Systems*, vol. 27, Curran Associates, Inc., 2014.
- [28] Andrew Gracyk and Xiaohui Chen, *Geonet: a neural operator for learning the Wasserstein geodesic*, *Proceedings of the Fortieth Conference on Uncertainty in Artificial Intelligence*, vol. 244, PMLR, 2024, pp. 1453–1478.
- [29] Ishaan Gulrajani, Faruk Ahmed, Martin Arjovsky, Vincent Dumoulin, and Aaron C Courville, *Improved training of Wasserstein GANs*, *Advances in Neural Information Processing Systems*, vol. 30, Curran Associates, Inc., 2017.
- [30] Daisuke Inoue, Yuji Ito, and Hiroaki Yoshida, *Optimal transport-based coverage control for swarm robot systems: Generalization of the Voronoi tessellation-based method*, *IEEE Control Systems Letters* **5** (2020), no. 4, 1483–1488.
- [31] Leonid Kantorovitch, *On the translocation of masses*, *Management Science* **5** (1958), no. 1, 1–4.

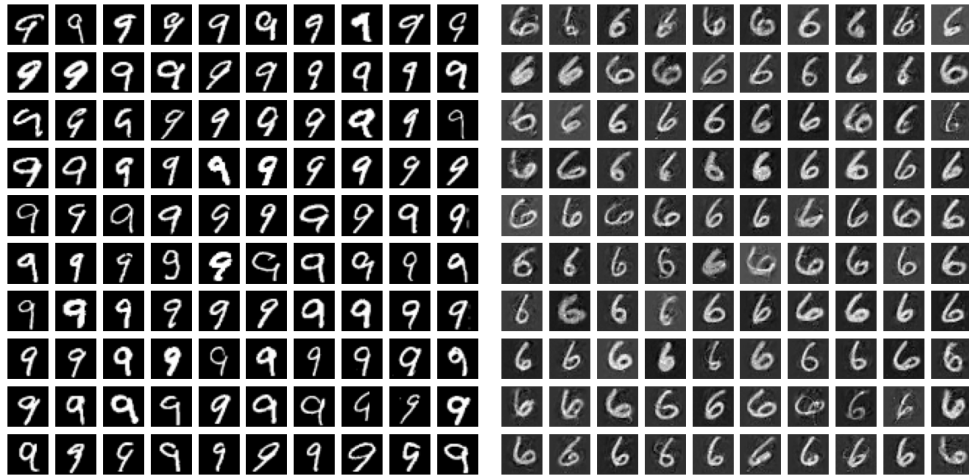


FIGURE 9. Phase 1 of Real data (MNIST): Left panel contains 100 samples from the source distribution ρ_a (digit 9). Right panel consists of transported samples $G_\theta(1; \cdot)_{\#\rho_a}$, which is meant to match ρ_b (digit 6).

- [32] Alexander Korotin, Vage Egiazarian, Arip Asadulaev, Alexander Safin, and Evgeny Burnaev, *Wasserstein-2 generative networks*, International Conference on Learning Representations, 2021.
- [33] Alexander Korotin, Lingxiao Li, Aude Genevay, Justin M Solomon, Alexander Filippov, and Evgeny Burnaev, *Do neural optimal transport solvers work? a continuous Wasserstein-2 benchmark*, Advances in neural information processing systems **34** (2021), 14593–14605.
- [34] Alexander Korotin, Daniil Selikhanovych, and Evgeny Burnaev, *Neural optimal transport*, The Eleventh International Conference on Learning Representations, 2023.
- [35] Vishaal Krishnan and Sonia Martínez, *Distributed optimal transport for the deployment of swarms*, 2018 IEEE Conference on Decision and Control (CDC), IEEE, 2018, pp. 4583–4588.
- [36] Yann LeCun, Léon Bottou, Yoshua Bengio, and Patrick Haffner, *Gradient-based learning applied to document recognition*, Proceedings of the IEEE **86** (1998), no. 11, 2278–2324.
- [37] Jacob Leygonie, Jennifer She, Amjad Almahairi, Sai Rajeswar, and Aaron Courville, *Adversarial computation of optimal transport maps*, arXiv preprint arXiv:1906.09691 (2019).
- [38] Wuchen Li, Ernest K Ryu, Stanley Osher, Wotao Yin, and Wilfrid Gangbo, *A parallel method for earth mover’s distance*, Journal of Scientific Computing **75** (2018), no. 1, 182–197.
- [39] Huidong Liu, Xianfeng Gu, and Dimitris Samaras, *Wasserstein GAN with quadratic transport cost*, Proceedings of the IEEE/CVF international conference on computer vision, 2019, pp. 4832–4841.
- [40] Huidong Liu, Gu Xianfeng, and Dimitris Samaras, *A two-step computation of the exact GAN Wasserstein distance*, International Conference on Machine Learning, PMLR, 2018, pp. 3159–3168.
- [41] Shu Liu, Shaojun Ma, Yongxin Chen, Hongyuan Zha, and Haomin Zhou, *Learning high dimensional Wasserstein geodesics*, arXiv preprint arXiv:2102.02992 (2021).
- [42] Guansong Lu, Zhiming Zhou, Jian Shen, Cheng Chen, Weinan Zhang, and Yong Yu, *Large-scale optimal transport via adversarial training with cycle-consistency*, arXiv preprint arXiv:2003.06635 (2020).
- [43] Ashok Makkuva, Amirhossein Taghvaei, Sewoong Oh, and Jason Lee, *Optimal transport mapping via input convex neural networks*, International Conference on Machine Learning, PMLR, 2020, pp. 6672–6681.
- [44] Takeru Miyato, Toshiki Kataoka, Masanori Koyama, and Yuichi Yoshida, *Spectral normalization for generative adversarial networks*, International Conference on Learning Representations, 2018.
- [45] Gaspard Monge, *Mémoire sur la théorie des déblais et des remblais*, Mem. Math. Phys. Acad. Royale Sci. (1781), 666–704.

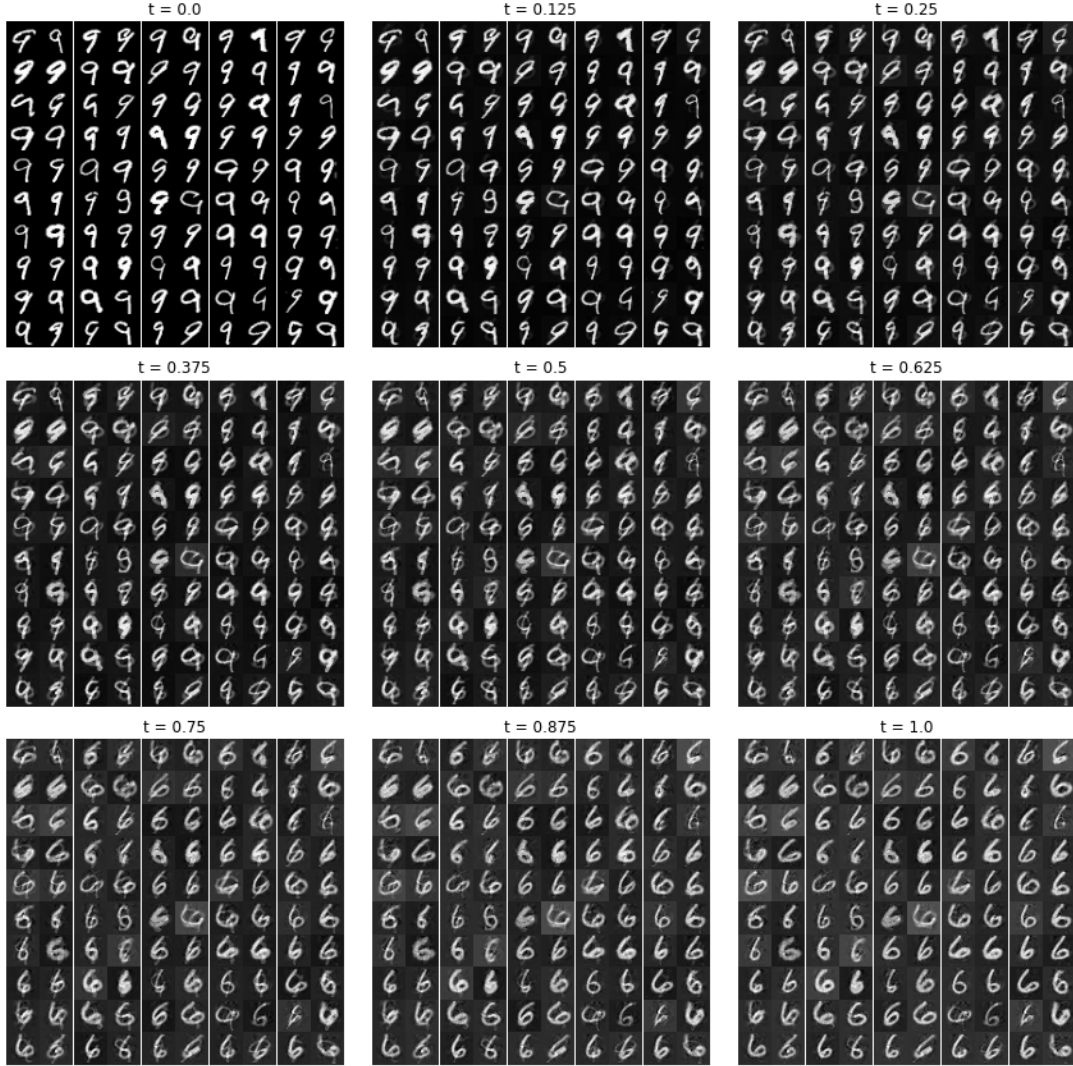


FIGURE 10. Phase 1 of Real data case (MNIST): Selected time slices of the transformation process from ρ_a (digit 9) to $G_\theta(1; \cdot)_{\# \rho_a}$, which is meant to match ρ_b (digit 6).

- [46] Gabriel Peyré and Marco Cuturi, *Computational optimal transport: With applications to data science*, Foundations and Trends in Machine Learning **11** (2019), no. 5-6, 355–607.
- [47] Litu Rout, Alexander Korotin, and Evgeny Burnaev, *Generative modeling with optimal transport maps*, Proceedings of the International Conference on Learning Representations, 2022.
- [48] Geoffrey Schiebinger, Jian Shu, Marcin Tabaka, Brian Cleary, Vidya Subramanian, Aryeh Solomon, Joshua Gould, Siyan Liu, Stacie Lin, Peter Berube, Lia Lee, Jenny Chen, Justin Brumbaugh, Philippe Rigollet, Konrad Hochedlinger, Rudolf Jaenisch, Aviv Regev, and Eric S. Lander, *Optimal-transport analysis of single-cell gene expression identifies developmental trajectories in reprogramming*, Cell **176** (2019), no. 4, 928–943.
- [49] Vivien Seguy, Bharath Bhushan Damodaran, Remi Flamary, Nicolas Courty, Antoine Rolet, and Mathieu Blondel, *Large-scale optimal transport and mapping estimation*, ICLR 2018-International Conference on Learning Representations, 2018, pp. 1–15.
- [50] Justin Solomon, Fernando de Goes, Gabriel Peyré, Marco Cuturi, Adrian Butscher, Andy Nguyen, Tao Du, and Leonidas J. Guibas, *Convolutional Wasserstein distances: Efficient optimal transportation on geometric domains*, ACM Transactions on Graphics **34** (2015), no. 4, 66:1–66:11.

- [51] Zhengyu Su, Yalin Wang, Rui Shi, Wei Zeng, Jian Sun, Feng Luo, and Xianfeng Gu, *Optimal mass transport for shape matching and comparison*, IEEE Transactions on Pattern Analysis and Machine Intelligence **37** (2015), no. 11, 2246–2259.
- [52] Tijmen Tieleman, *Lecture 6.5-RMSProp: Divide the gradient by a running average of its recent magnitude*, COURSERA: Neural Networks for Machine Learning **4** (2012), no. 2, 26.
- [53] Cédric Villani, *Optimal transport: old and new*, vol. 338, Springer, 2008.
- [54] ———, *Topics in optimal transportation*, vol. 58, American Mathematical Soc., 2021.
- [55] Xiang Wei, Boqing Gong, Zixia Liu, Wei Lu, and Liqiang Wang, *Improving the improved training of Wasserstein GANs: A consistency term and its dual effect*, International Conference on Learning Representations, 2018.
- [56] Yujia Xie, Minshuo Chen, Haoming Jiang, Tuo Zhao, and Hongyuan Zha, *On scalable and efficient computation of large scale optimal transport*, International Conference on Machine Learning, PMLR, 2019, pp. 6882–6892.

APPENDIX A. PROOF OF CONSISTENCY

We show that problem (2.6) is equivalent to problem (2.2) by proving the following identity

$$\inf_F \sup_{\phi: \text{Lip}} f_1(G) + f_2(G, \phi) = \inf_{G: W(G(1; \cdot) \# \rho_a, \rho_b) = 0} f_1(G),$$

where

$$\begin{aligned} G(t; z) &= z + tF(z, t), \\ f_1(G) &:= \mathbb{E} \left[L \left(\frac{dG(U; Z)}{dt} \right) \right], \\ f_2(G, \phi) &:= \mathbb{E} [\phi(G(1; Z))] - \mathbb{E} [\phi(Y)]. \end{aligned}$$

Assume the min-max problem (2.6) admits a unique solution (F^*, ϕ^*) , and define

$$G^*(t; z) := z + tF^*(z, t).$$

Let ϕ be any Lipschitz function. By triangle inequality, both $\phi^* + \phi$ and $\phi^* - \phi$ are also Lipschitz functions. In particular, since $\phi^* + \phi$ is Lipschitz, we have

$$\begin{aligned} f_1(G^*) + f_2(G^*, \phi^* + \phi) &\leq f_1(G^*) + f_2(G^*, \phi^*) \\ \Rightarrow f_2(G^*, \phi^* + \phi) - f_2(G^*, \phi^*) &\leq 0. \\ \Rightarrow \mathbb{E} [\phi^*(G^*(1; Z)) + \phi(G^*(1; Z))] - \mathbb{E} [\phi^*(Y) + \phi(Y)] - \mathbb{E} [\phi^*(G^*(1; Z))] + \mathbb{E} [\phi^*(Y)] &\leq 0 \\ \Rightarrow \mathbb{E} [\phi(G^*(1; Z))] - \mathbb{E} [\phi(Y)] &\leq 0. \end{aligned}$$

Since $\phi^* - \phi$ is also a Lipschitz function, we can apply the same argument as above to obtain

$$\mathbb{E} [\phi(G^*(1; Z))] - \mathbb{E} [\phi(Y)] \geq 0,$$

which implies that

$$f_2(G^*, \phi) = \mathbb{E} [\phi(G^*(1; Z))] - \mathbb{E} [\phi(Y)] = 0 \text{ for all Lipschitz } \phi.$$

By the Kantorovich-Rubinstein duality (2.4), we then have

$$W(G^*(1; \cdot) \# \rho_a, \rho_b) = \sup_{\phi: 1\text{-Lip}} \mathbb{E} [\phi(G^*(1; Z))] - \mathbb{E} [\phi(Y)] = \sup_{\phi: 1\text{-Lip}} f_2(G^*, \phi) = 0$$

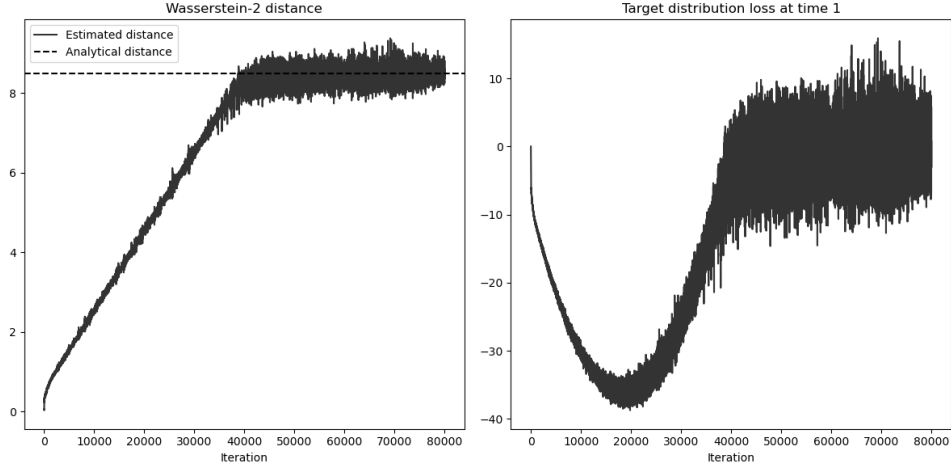


FIGURE 11. Synthetic-1, Phase 1: The left panel shows the estimated $W_2(\rho_a, \rho_b)$ over training iterations; the dash line refers to the analytical value. The right panel shows the estimated $W_1(G_\theta(1; \cdot)_{\#}\rho_a, \rho_b)$ over iterations.

Finally, we conclude the proof by showing the equivalence of the min-max and constrained formulations:

$$\begin{aligned}
 \inf_F \sup_{\phi: \text{Lip}} f_1(G) + f_2(G, \phi) &= \sup_{\phi: \text{Lip}} \inf_F f_1(G) + f_2(G, \phi) \\
 &= \sup_{\phi: \text{Lip}} f_1(G^*) + f_2(G^*, \phi) \\
 &= \sup_{\phi: \text{Lip}} f_1(G^*) \\
 &= f_1(G^*) \\
 &= \inf_{G: W(G(1; \cdot)_{\#}\rho_a, \rho_b)=0} f_1(G),
 \end{aligned}$$

where the third line follows from the assumption that (F^*, ϕ^*) is the unique saddle point and $f_2(G^*, \phi) = 0$ for all Lipschitz ϕ , as shown above.

APPENDIX B. DETAILS OF NUMERICAL EXPERIMENTS

In this section, we report the evolution of the objective functions over the training iteration in each experiment.

B.1. Synthetic-1. Figure 11 tracks individual terms of the objective function (2.7) in Phase 1 over the training iterations. Fig 12 presents the loss of the objective function (3.1) in Phase 2 over the training iterations. Since the analytical velocity field v^* is available for this case, so we additionally report the mean squared error between $v_\eta(x, t)$ and $v^*(x, t)$ over the domain $x \in (-3, 10.9) \times (-3, 10.9)$ and $t \in (0, 1)$.

B.2. Synthetic-2. Fig 13 tracks individual terms of the objective function (2.7) in Phase 1 over the training iterations. Fig 14 presents the loss of the objective function (3.1) in Phase 2 over training iterations.

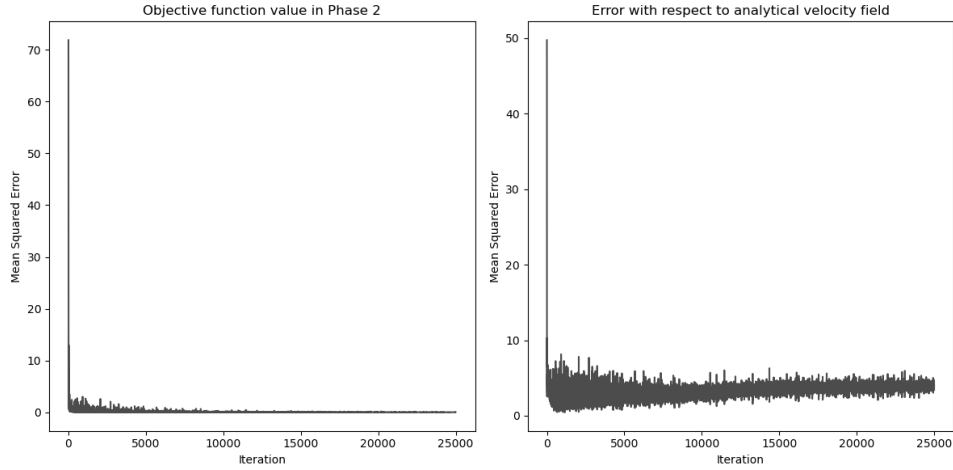


FIGURE 12. Synthetic-1, Phase 2: The left panel shows the loss of objective function value. The right panel shows the mean squared error between the learned velocity field v_η and the analytical one v^* .

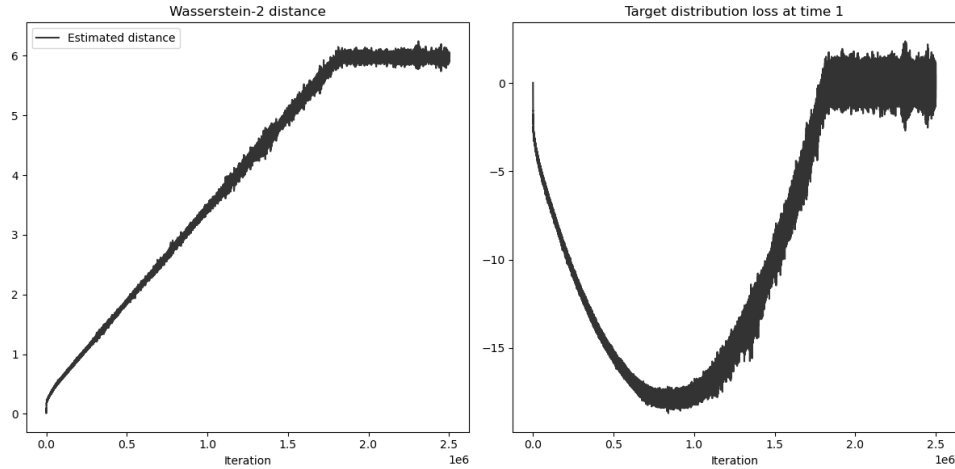


FIGURE 13. Synthetic-2, Phase 1: The left panel shows the estimated $W_2(\rho_a, \rho_b)$ over training iterations; the dash line refers to the analytical value. The right panel shows the estimated $W_1(G_\theta(1; \cdot) \# \rho_a, \rho_b)$ over iterations.

B.3. Synthetic-3. Fig 15 tracks individual terms of the objective function (2.7) in Phase 1 over the training iterations. Fig 16 presents the loss of the objective function (3.1) in Phase 2 over the training iterations. As in Synthetic-1, the analytical velocity field v^* is available for this case, so we additionally report the mean squared error between $v_\eta(x, t)$ and $v^*(x, t)$ over 100000 random points in a 10-dimensional hyperrectangle containing the means of the two functions.

B.4. Synthetic-4. Fig 17 tracks the objective function loss (2.7) in Phase 1 over training iterations. Fig 18 presents the corresponding loss of the objective function (3.1) in Phase

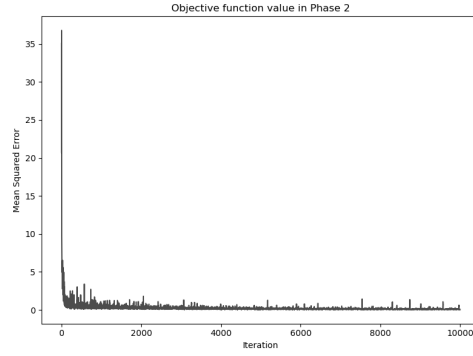


FIGURE 14. Synthetic-2, Phase 2: Loss of the objective function value.

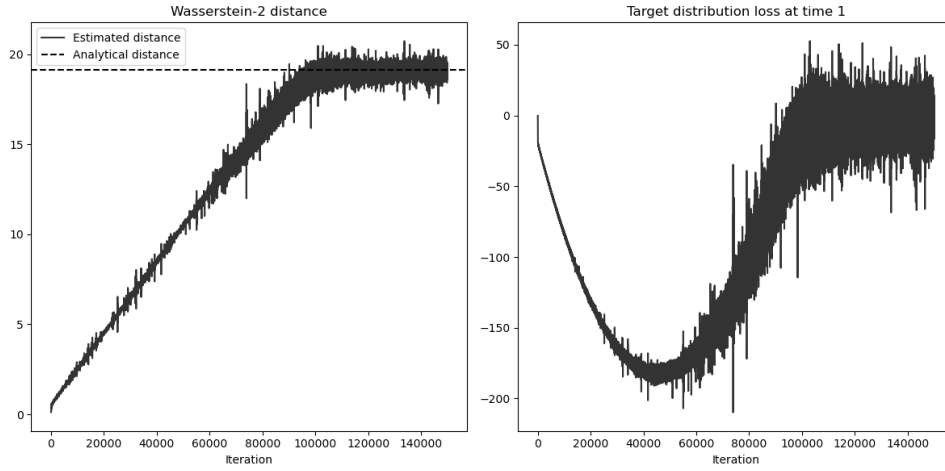


FIGURE 15. Synthetic-3, Phase 1: The left panel shows the estimated $W_2(\rho_a, \rho_b)$ over training iterations; the dash line refers to the analytical value. The right panel shows the estimated $W_1(G_\theta(1; \cdot) \# \rho_a, \rho_b)$ over iterations.

2 during training iterations.

B.5. Real data (MNIST). Fig 19 tracks the loss of the objective function (2.7) in Phase 1 over the training iterations. Fig 20 tracks the loss of the objective function (3.1) in Phase 2 over iterations.

Email address: yanhanc@iastate.edu

Email address: hliu@iastate.edu

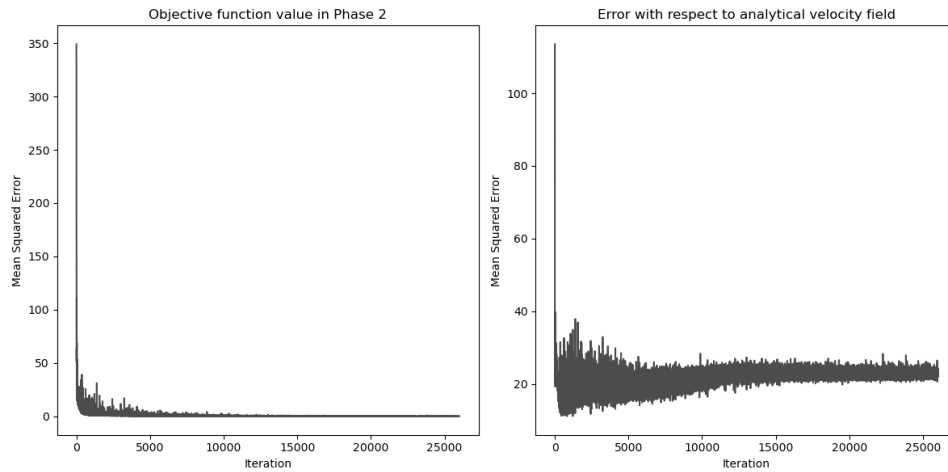


FIGURE 16. Synthetic-3, Phase 2: The left panel shows the loss of objective function value. The right panel shows the mean squared error between the learned velocity field v_η and the analytical one v^*

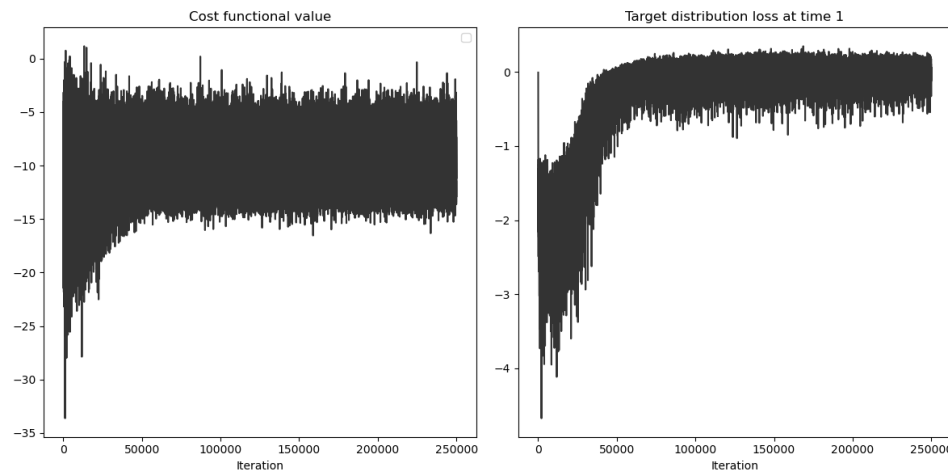


FIGURE 17. Synthetic-4: The left panel shows the estimated cost over training iterations. The right panel shows the estimated $W_1(G_\theta(1; \cdot) \# \rho_a, \rho_b)$ over iterations.

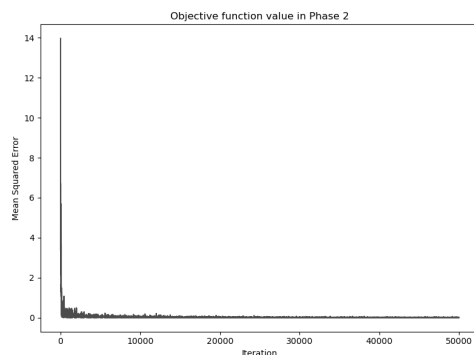


FIGURE 18. Synthetic-4: Loss of the objective function value.

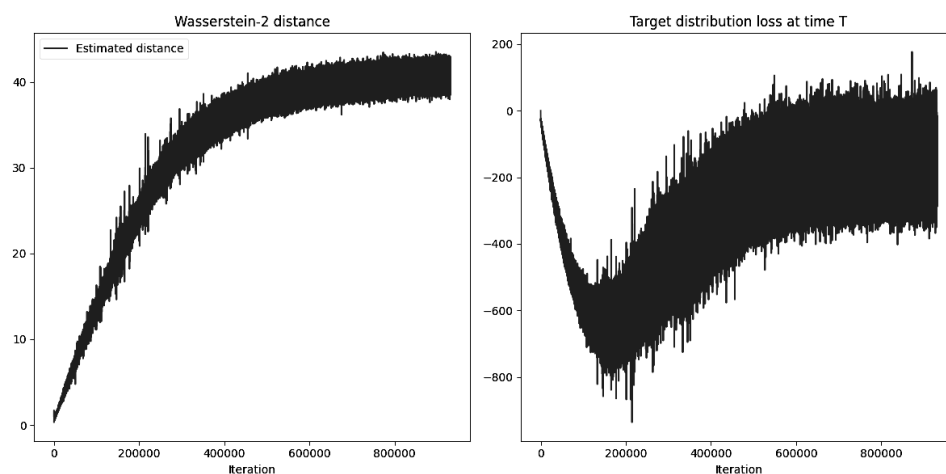
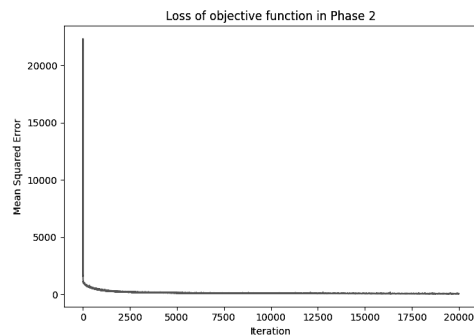
FIGURE 19. Realistic case: The left panel shows the estimated $W_2(\rho_a, \rho_b)$ over training iterations. The right panel shows the estimated $W_1(G_\theta(1; \cdot) \# \rho_a, \rho_b)$ over iterations.

FIGURE 20. Realistic case, Phase 2: Loss of the objective function value.